J. Synchrotron Rad. (1998). **5**, 82–89

On High-Resolution Reciprocal-Space Mapping with a Triple-Crystal Diffractometer for High-Energy X-rays

K.-D. Liss,* A. Royer, T. Tschentscher, P. Suortti and A. P. Williams†

European Synchrotron Radiation Facility, BP 220, F-38043 Grenoble CEDEX, France. E-mail: liss@esrf.fr

(Received 7 May 1997; accepted 7 October 1997)

High-energy X-ray diffraction by means of triple-crystal techniques is a powerful tool for investigating dislocations and strain in bulk materials. Radiation with an energy typically higher than 80 keV combines the advantage of low attenuation with high resolution at large momentum transfers. The triple-crystal diffractometer at the High Energy Beamline of the European Synchrotron Radiation Facility is described. It is shown how the transverse and longitudinal resolution depend on the choice of the crystal reflection, and how the orientation of a reciprocal-lattice distortion in an investigated sample towards the resolution element of the instrument can play an important role. This effect is demonstrated on a single crystal of silicon where a layer of macro pores reveals satellites around the Bragg reflection. The resulting longitudinal distortion can be investigated using the high transverse resolution of the instrument when choosing an appropriate reflection.

Keywords: Laue geometry; bulk measurements; perfect crystals; lateral modulated structures; satellite peaks.

1. Introduction

With the development of modern synchrotron sources, high-energy X-ray diffraction is starting to play an important role in the bulk analysis of materials. Since the absorption lengths above 100 keV for most materials lie in the 0.1 mm to several centimeter range, studies on thick samples as applied for materials research become accessible. For the same reason, window materials and thicknesses for sample environments such as cryostats or furnaces are less critical or negligible. Fig. 1 shows the attenuation lengths as a function of energy for the fifth element group representing the typical behaviour for each period. Clearly, photoabsorption, Compton scattering and pair production can be distinguished as dominating attenuation processes by the different slopes of the curves. Above 80 keV, silicon suffers even weaker attenuation than diamond due to a higher Compton contribution for the latter. For heavier elements, photoabsorption still dominates at 100 keV, but crystals in the millimeter range containing lead are easily accessible below the K edge. Last but not least, diffraction becomes weaker with increasing energies, which allows kinematical rather than dynamical treatment in the study of almost perfect crystals. Here, for example, energies from 300 to 500 keV have been used to study lattice distortions induced by ultrasound (Liss, Magerl, Remhof & Hock, 1997).

† Now at Phoenix Technologies SARL, F-74160 Archamps, France.

Investigations of crystal perfection using triple-crystal diffractometry provide the highest resolution in both longitudinal and transverse directions with respect to the scattering vector. Studies of reciprocal space with this kind of instrument at lower energies have been known for many years (Pick *et al.*, 1977), whereas the resolution function of the high-energy machines has only been discussed more recently (Neumann, 1991; Neumann *et al.*, 1994; Rütt *et al.*, 1995). Investigations of lattice distortions in perfect (Liss

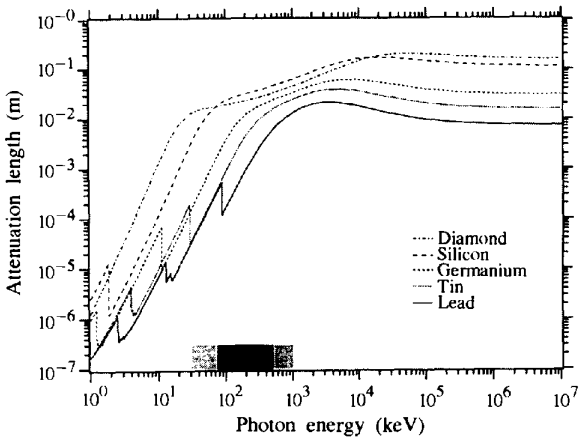

Figure 1
Attenuation lengths for the elements of the fifth period as a function of energy. The light-grey energy range between 30 keV and 1 MeV is accessible at ESRF beamline ID15, and the dark-grey region shows the typical range of operation of the triple-axis diffractometer.

et al., 1996; Liss, Magerl, Hock *et al.*, 1997; Liss, Magerl, Remhof & Hock, 1997) and imperfect materials (Liss, 1994; Magerl *et al.*, 1995; Bouchard *et al.*, 1993; Helmers, 1996), studies of macroscopic thick samples (Royer *et al.*, 1997*a*,*b*; Royer & Bastie, 1997), structural phase transitions in the bulk (Poulsen *et al.*, 1996; Neumann *et al.*, 1995), diffuse diffraction from relaxor ferroelectrics (Zhukov *et al.*, 1995), non-resonant magnetic diffraction (Lippert *et al.*, 1994; Strempfer *et al.*, 1996), and anomalous thermal expansion near a magnetic phase transition (Chattopadhyay *et al.*, 1997) are only a few of the applications that have already used this technique. In this article we describe the newly installed triple-crystal diffractometer at the High Energy Beamline of the ESRF and discuss, in particular, the choice of the sample reflection, which plays an important role in reciprocal-space mapping when the highest resolution is demanded.

2. Triple-crystal diffractometer

The instrument is a permanent installation at the high-energy beamline ID15A at the ESRF; Fig. 2 shows the scattering plane seen from above. A small white beam arrives from the left from one of the insertion devices, either the asymmetric wiggler or the superconducting wavelength shifter (Suortti & Tschentscher, 1995). The insertion devices have been optimized for the use of high energies, with critical energies, E_C, equal to 45 and 96 keV, and the incident beam is attenuated permanently by 4 mm Al, 3.5 mm Be and 1 mm C to reduce the heat load on the monochromator crystal. The scattering plane is horizontal and the rotation tables for the monochromator (M), sample (S) and analyzer (A) are mounted on a large optical table, each on a translation stage. Each rotation axis consists of a coarse rotation and a high-resolution rotation. The coarse rotations are DC-motor-driven to provide fine smooth movements, and the fine rotations are provided by piezo-actuators, which are coupled by weak link devices. For the sample axis the coarse motor can be replaced by a stepper motor in order to provide faster rotation for samples with larger mosaicity or for investigations of the full reciprocal space. The energy-dispersive Ge detector is positioned on an extra bench behind the table. When high-indexed reflections are used, crystal rocking curves become very narrow at high energies and it is important to control the position of the rotation axes very precisely. It is furthermore crucial to provide a system that monitors the movements of all three rotation axes simultaneously, because the relative orientation of the three crystals has a significant effect on the intensity at the detector. A laser interferometer (I) is therefore mounted onto a glass ceramic table on top of the optical table. Its three individual interferometer set-ups monitor the movements of each axis by changes in the optical path induced by mirrors which are mounted on the rotation tables. The system uses a single laser source and signals are detected for each rotation axis independently. A feedback system, which reads these detector signals and controls piezo-actuators used for the fine rotation, assures a long time stability of 0.1″ over an angular range of ±10°.

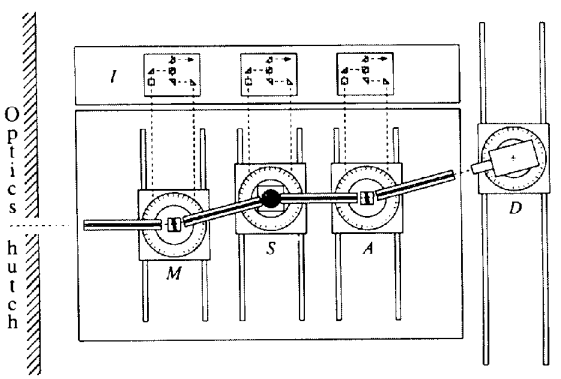

Figure 2
The triple-crystal diffractometer at beamline ID15A at the ESRF. The monochromator, M, sample, S, analyzer, A, and detector, D, axes are mounted on translation rails to drive the rotation centers into the beams. Interferometers, I, read and control the angular positions of the crystals M, S and A.

3. Interferometric encoders

An individual interferometer for the control of one axis is shown in Fig. 3. A beam of an He–Ne laser with a mean wavelength of λ = 633 nm enters through a tunnel under the prism, $P1$, on the beam splitter, BS. Here, half of the intensity is transmitted to pass through prisms $P2$ and $P3$ onto the left corner-cube prism, $CC1$, of the lever arm, L, which is fixed to the rotation axis, R. The corner-cube prism has the property of reflecting the beam back parallel

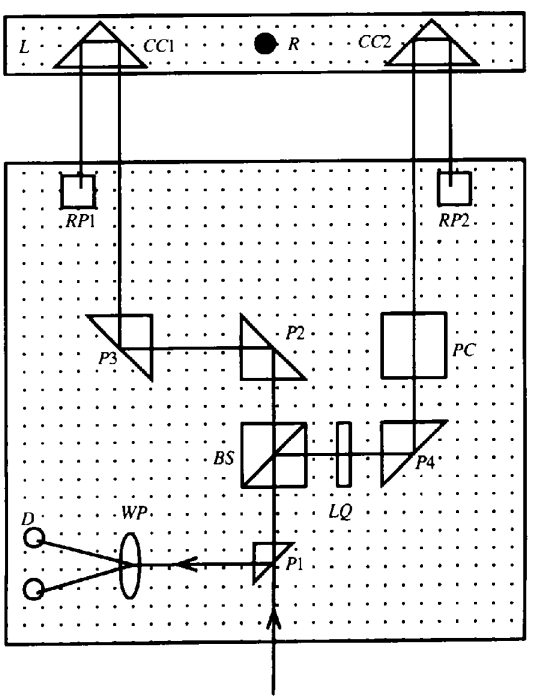

Figure 3
Schematic layout of one of the three identical interferometers.

but displaced relative to its incoming direction regardless of the prism's orientation. Since the outgoing beam is shifted towards the left, it hits the roof prism, $RP1$, which then reflects back through the whole path of the optics, but in a plane 10 mm above the plane of incidence. The other half of the intensity split in the beam splitter is reflected to the prism $P4$ and passes an optical path compensator, PC, to hit the lever arm, L, on the right-hand side. Similar optics for the left-hand side ensure that the beam from both paths interferes in the beam splitter and is finally reflected by $P1$ into the detector system, D. When the lever arm rotates counterclockwise around R by an angle θ, the distance $CC1$–$RP1$ shortens by $L/2 \sin\theta$, while the distance $CC2$–$RP2$ enlarges by the same amount, L being the distance between the corner cubes on the lever arm. As on both sides of the interferometer the laser beam traverses the path from the lever arm to the interferometer base plate four times, the phases of the split beams change by

$$\Delta\Phi_l = -2kL\sin\theta \tag{1}$$

and

$$\Delta\Phi_r = 2kL\sin\theta + \delta_0, \tag{2}$$

where $k = 2\pi/\lambda$ and δ_0 is a constant phase factor introduced by the phase shifter, LQ, in the outgoing part of the right-hand side of the interferometer. Therefore, the time-independent part of the interfering waves has the form

$$\psi(\theta) = \exp[i(2kL\sin\theta) + \delta_0] + \exp[-i(2kL\sin\theta)]. \tag{3}$$

For the intensity $I(\theta) = \psi(\theta)\psi^*(\theta)$, this yields

$$I(\theta) = 2 + 2\cos(4kL\sin\theta). \tag{4}$$

The rotation angle is detected by counting the interference fringes, *i.e.* the oscillation (4) during the motion. With a length $L = 20$ cm of the interferometer arm, one fringe corresponds to 0.16″.

Using one fringe as the step size still does not give the necessary resolution for high-energy X-ray diffraction. Furthermore, one cannot be sure in which direction the axis rotates. However, a conceptionally simple trick, the so-called piggyback method, allows this difficulty to be overcome. Suppose, instead of using only one interferometer, there are two and an additional phase shift of 90° is introduced in one of the arms of the second interferometer. Then the signals at the two photodetectors are

$$I_1(\theta) = 2 + 2\cos(4kL\sin\theta) \tag{5}$$

and

$$I_2(\theta) = 2 + 2\sin(4kL\sin\theta). \tag{6}$$

From the signs of the two signals, sign $(I_1 - 2)$ and sign $(I_2 - 2)$, one can determine in which quadrant the phase difference $\Delta\Phi = 4kL\sin\theta$ lies. One can also determine the direction in which this phase difference changes, as shown in Table 1.

Table 1
Directions of phase-difference changes.

Sign $(I_1 - 2)$	Sign $(I_2 - 2)$ changes from → to	Direction of change of $\Delta\Phi$
+	− → +	Increase
+	+ → −	Decrease
−	− → +	Decrease
−	+ → −	Increase

The layout of such a double interferometer makes use of the linear polarization of the laser light. The light is polarized by a prism such that the plane of polarization is at an angle of 45 so that the vertically and horizontally polarized components have equal intensity. A $\lambda/4$ plate, LQ, is inserted into one of the interferometer arms. The consequence is that in this arm an additional shift of $\pi/4$ is added to the phase of one of the polarization directions. On leaving the interferometer the two polarizations are spatially separated by a Wollaston prism, WP, and recorded independently by two photon detectors.

Electronically the detection is realized by two Schmitt triggers transforming the sinusoidal signals into a digital high/low level. A standard up–down counter registers the position. Thus, the rotation angle can be determined to an accuracy of 0.04″. A deviation from the set point is detected if the counter differs by ±1 and a VME-based digital feedback corrects the deviation by driving the piezoelectric actuator that is employed for fine adjustment. This regulation system gives a stability of 0.1″.

4. Scanning procedure

The situation in reciprocal space is shown in Fig. 4. The monochromator defines the incident wavevector, $\mathbf{k}_i$, in both modulus and direction, and the analyzer probes the observed wavevector, $\mathbf{k}_f$. If the sample provides a scattering vector, $\mathbf{G} = \mathbf{k}_f - \mathbf{k}_i$ intensity reaches the detector. The distribution of scattering vectors in the scattering plane

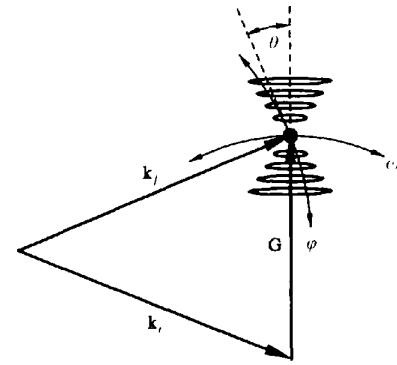

Figure 4
Principle of two-dimensional mapping of a reciprocal-lattice-vector distribution by a grid scan of the sample and the analyzer axes ω and φ, respectively. The monochromator defines an incident wavevector $\mathbf{k}_i$, the analyzer looks for $\mathbf{k}_f$ and intensity passes to the detector depending on the distribution of the scattering vector $\mathbf{G}$.

can be probed by two linearly independent motions in the common scattering plane, firstly by a rotation of the sample around the ω axis and secondly by rotating the analyzer crystal around the φ axis. The former rotation corresponds to a scan perpendicular to the scattering vector and one derives from the figure

$$(\Delta G_\perp/G)|_\omega = \Delta\omega, \tag{7}$$

with $G = |\mathbf{G}|$. This scan is usually applied to measure the mosaic spread of the sample for a fixed scattering-vector length. The second motion rotates $\mathbf{k}_f$ and one scans along a line which is inclined by the Bragg angle, θ, against the longitudinal direction. Both longitudinal and transverse components are varied and one obtains, for fixed ω,

$$(\Delta G_{||}/G)|_\varphi = (k/G)\Delta\varphi\cos\theta = \Delta\varphi/(2\tan\theta) \tag{8}$$

and

$$(\Delta G_\perp/G)|_\varphi = (k/G)\Delta\varphi\sin\theta = \Delta\varphi/2. \tag{9}$$

Thus, intensity maps measured in the sheared instrument coordinate system $(\Delta\varphi, \Delta\omega)$ have to be transformed *via*

$$\begin{pmatrix} \Delta G_{||}/G \\ \Delta G_\perp/G \end{pmatrix} = \begin{pmatrix} 1/2\tan\theta & 0 \\ 1/2 & 1 \end{pmatrix} \begin{pmatrix} \Delta\varphi \\ \Delta\omega \end{pmatrix} \tag{10}$$

to the local Cartesian coordinates around the main scattering vector, **G**.

The rocking width of a Bragg reflection of a perfect crystal is given by

$$\Delta\theta_D = 16\pi K r_e F(f)\tan\theta/(|b|^{1/2}V_z G^2), \tag{11}$$

according to the dynamical theory of diffraction (Zachariasen, 1945; Rauch & Petrascheck, 1976, 1978). Here, r_e is the classical electron radius, $F(f)$ is the structure factor containing the form factor f, V_z is the volume of the unit cell, $b = \cos\gamma_0/\cos\gamma_G$, the ratio of the direction cosines, and $K = 1$ for σ-polarization or $K = \cos 2\theta$ for π-polarization. Bragg angles for high energies are small, thus K is close to unity for both cases. To calculate the resolution of the instrument for the case of three identical crystal reflections in $(+-+)$ geometry, *i.e.* the non-dispersive setup, one has to set $\Delta\varphi = 2\Delta\theta_D$ and $\Delta\omega = 2\Delta\theta_D$, the factor of two being a convolution factor arising from the Lorentzian-shaped reflectivity curve of a single reflection, and to apply the transformation (10). One recognizes immediately that the transverse resolution scales with the X-ray energy when θ decreases. The longitudinal resolution, however, does not show this dependence since the $\tan\theta$ term from (11) vanishes in (10) and (8). There is no means

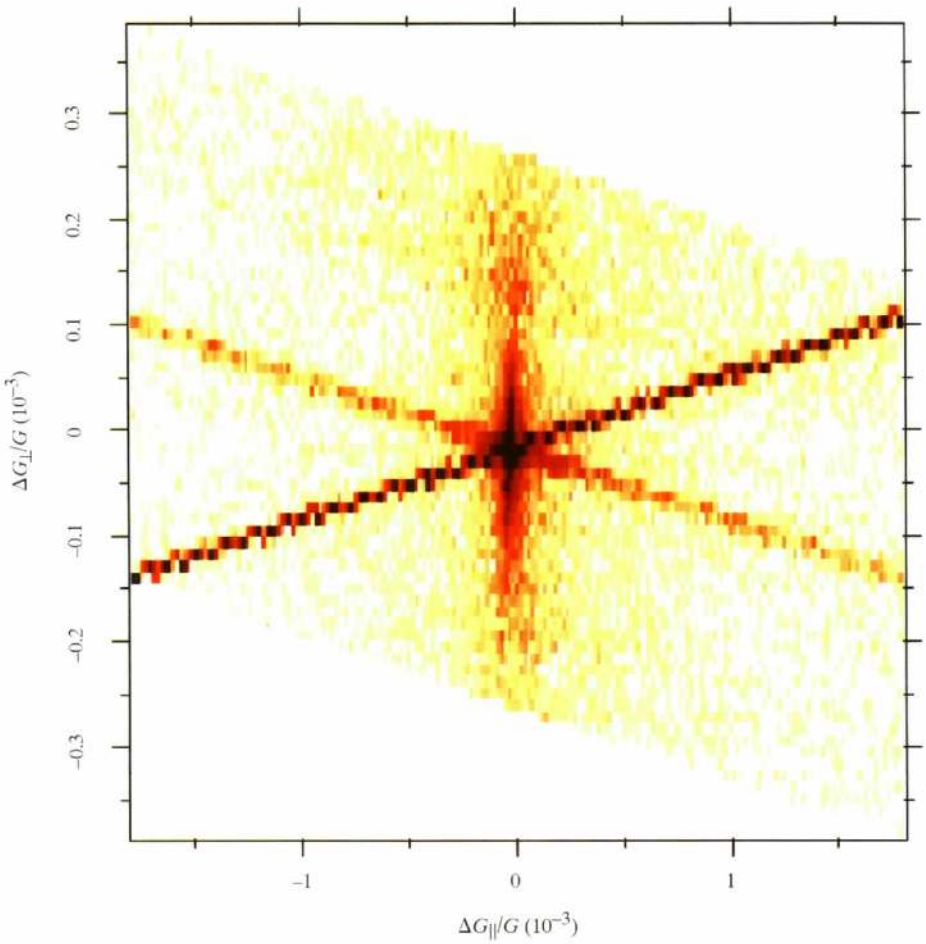

Figure 5
Measured resolution streaks at the Si $\bar{3}51$ reflection at 100 keV. The linearity of the streaks demonstrates the long time stability (15 h) of the instrument.

to change the longitudinal resolution apart from changing the reflections. With higher Miller indices, G increases in the denominator of (11) and additionally f decreases in the numerator. For high orders and high energies, $2\Delta\theta_D$ drops rapidly below the long-term stability (0.1″) of our instrument, which limits the indices for silicon reflections to 731 or 553 at 100 keV and 331 or 422 at 300 keV, corresponding to longitudinal resolutions of 2.8×10^{-6} and about 1.5×10^{-5}, respectively. This demonstrates that longitudinal resolution and penetration power have to be compromised.

The instrument resolution functions have been discussed in detail by the HASYLAB group (Neumann *et al.*, 1994; Rütt *et al.*, 1995) for the non-dispersive and the general set-ups, respectively. Fig. 5 shows, as an example, the resolution function obtained with the ESRF instrument using three perfect Si crystals in the $\bar{3}51$ reflection at 100 keV. Even with insufficient statistical accuracy of the data and the large step width of 0.25″ for φ, compared with a line width $\Delta\theta_D = 0.087''$, the three resolution streaks that are typical of the instrument can be easily recognized. Monochromator and analyzer streaks, here the latter being the more intense, are each inclined by the Bragg angle $\theta = 3.87°$ towards the longitudinal direction, whereas the sample streak follows the transverse component of reciprocal space. The scan was intended for the commissioning of the interferometric encoders and the straight streaks demonstrate the long time stability of the instrument over 15 h.

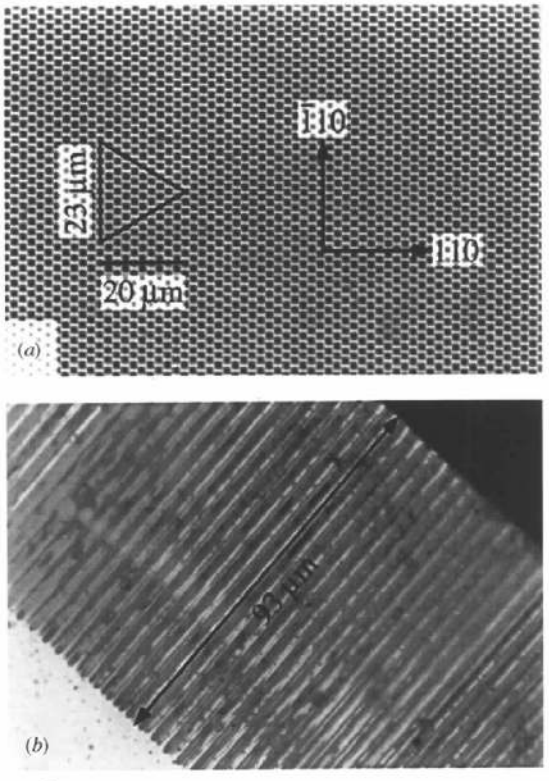

Figure 6
Top view (*a*) and section (*b*) of the macroporous sample. The holes of the triangular grid are each 93 µm deep and 2.3 µm in periodicity. The top surface coincides with the 001 direction of the crystal lattice.

5. Sample description

The sample studied in this paper is a layer of silicon with a pattern of micro-machined pores. It was manufactured by the research laboratories of Siemens AG for the study of two-dimensional photonic band structures. It consists of a silicon wafer of thickness 530 µm with a regular macro structure etched from one of its (001) surfaces. An electrochemical etching procedure was used for its production. Overview articles concerning this sample have been given by Grüning, Lehmann & Eberl (1996) and Grüning, Lehmann, Ottow & Busch (1996). The structure, shown by the micro photographs in Fig. 6, consists of a two-dimensional periodic triangular lattice of square holes, all about 1.8 µm (L) × 1.8 µm (W), 93 µm deep and 2.3 µm in periodicity. The dimensions of the walls between the pores are one order of magnitude less. The superlattice can be described by a rectangular grid with two holes per unit cell. Then the basis vectors of the super unit cell coincide with the $\bar{2}20$ and 220 directions of the atomic lattice and their lengths are 2.3 and 4.0 µm, respectively. The stacking orders in the hole columns and rows are *AAAA* and *ABAB*, respectively.

6. Reciprocal-space mapping

The orientation of the sample and the reciprocal-lattice vectors are sketched in Fig. 7. Owing to the periodicity, satellites around the Bragg peaks are expected to be distributed along the 110 direction. Therefore, we first chose the 220 reflection for reciprocal-space mapping at 125 keV (Fig. 8). Nevertheless, no satellites were seen in the two-

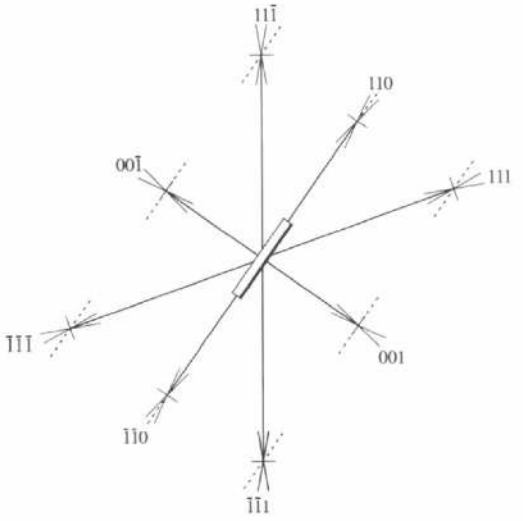

Figure 7
Reciprocal-lattice points with expected satellites illustrated around the section view of the sample. Resolution streaks are sketched around the reflections showing qualitatively that the satellites lie most favourably for a scan around the 11$\bar{1}$ point.

crystal mode, which integrates over the longitudinal component. In the three-crystal mode an additional streak appears between the analyzer and monochromator streaks which denotes the modulated 220 direction; however, satellites cannot be resolved. The resolution in the longitudinal direction is too poor. For higher resolution one has to aim for a streak direction into the empty quadrants of $(\Delta\varphi, \Delta\omega)$ space. Drawing the resolution streaks into the sketch (Fig. 7) for different reflections one finds the [001] direction to be best oriented. For an allowed multiple of this reflection, however, one is insensitive to longitudinal lattice-parameter variations within the modulation direction, and, particularly in the present case, one would measure in Bragg geometry which, for very small scattering angles, as they occur with high-energy X-rays, is a bad choice. Therefore, we choose the $[11\bar{1}]$ direction to be more adequate. Indeed, the mapping in Fig. 9 obtained at 80 keV shows the expected features. Each satellite lies on the $[\xi\xi 0]$ line starting from the $11\bar{1}$ point, is perfectly resolved and has individual resolution streaks. Even the transverse sample streak can be estimated and clearly does not coincide with the direction of the satellites. Fig. 10 presents the longitudinally integrated rocking scan and reveals 2×32 satellites within $300''$ on each side of the main peak and the oscillation seems to continue outside this range. The distance between two neighbour satellites is $\Delta\theta = 9.0''$.

The situation in the two-crystal mode is sketched in Fig. 11. Let the end point of the scattering vector, **G**, be on the Ewald sphere, S, and $\mathbf{G} + \Delta\mathbf{G}$ be the scattering vector corresponding to the first neighbour satellite. The magnitude of ΔG is the variable of interest and can be represented by a component parallel and perpendicular to the scattering vector,

$$\Delta G_{\parallel} = \Delta G \cos\alpha \tag{12}$$

and

$$\Delta G_{\perp} = \Delta G \sin\alpha, \tag{13}$$

respectively, α being the angle between the scattering vector and the direction of $\Delta\mathbf{G}$, *i.e.* $\alpha = 35.26^{\circ}$ between the $[11\bar{1}]$ and the [110] direction. A crystal rotation of $\Delta\theta$ is necessary to bring the considered satellite onto the Ewald sphere. From Fig. 11 it follows that

$$\Delta\theta = (\Delta G_{\perp} - \Delta g)/G. \tag{14}$$

Since the Ewald sphere is inclined by the Bragg angle $\theta = 1.43^{\circ}$ to the scattering vector,

$$\Delta g = \Delta G_{\parallel} \tan\theta \tag{15}$$

and thus

$$\Delta G = G\Delta\theta/(\sin\alpha - \cos\alpha \tan\theta). \tag{16}$$

For $\Delta\theta = 9.0'' = 4.36 \times 10^{-5}$ rad and $G = 2.00$ Å^{-1}, one obtains $\Delta G = 1.57 \times 10^{-4}$ Å^{-1}, corresponding to a real-space dimension of $d = 2\pi/\Delta G = 4.01$ µm. This result coincides perfectly with the periodicity of the *ABAB* direction of the macro lattice and demonstrates the reliability of the technique.

Although the exploitation of all the features of the spectrum is outside the scope of this article, we wish to mention the most relevant points with initial interpretations. For detailed evaluation strategies readers are referred to articles such as those by Shen (1996) and Shen & Kycia (1997). The main peak in Fig. 10 has a shoulder at $\Delta G = -1.4 \times 10^{-5}$ Å^{-1} and a width of 4.0×10^{-5} Å^{-1}, compared with the narrowest side peaks showing widths of 2.32×10^{-5} Å^{-1}, which is the convoluted intrinsic value of 2.327×10^{-5} Å^{-1} corresponding to $2\Delta\theta_D$. The shoulder and the enlarged width could be explained by a relative lattice-parameter expansion of 10^{-6} and a continuous lattice gradient, respectively. Additionally, a modulation of the individual satellite intensities suppressing the fifth side peaks at $\pm 0.78 \times 10^{-3}$ Å^{-1} on each side of the main maximum relates to a real-space dimension of 0.8 µm, which is roughly half the diameter of a pore. Every odd satellite counted from the main peak to the seventh is more weakly modulated than the even-numbered satellite, giving a Fourier component corresponding to double the satellite distance or half the spacing of the super lattice, which is the dimension of a single hole unit including its wall of 2.0 µm. The structured background changes its mean slope around the fifth side peak, which again relates to the dimension discussed above, but additionally it reveals a step at -4.1×10^{-3} Å^{-1} corresponding to 150 nm being the minimum thickness of the walls between the pores. An open question concerns the asymmetry in the structured background with more intensity and the aforementioned step observed on the side of smaller scattering vectors. This could probably be analysed in terms of missing electron density in the pores.

7. Conclusions

To obtain high-resolution mappings of reciprocal space it is of fundamental importance to orient the resolution element of the triple-crystal diffractometer appropriately. In particular, the high transverse resolution of a well chosen out-of-plane Bragg reflection can be used to resolve longitudinal variations of the in-plane direction, whereas direct access to the longitudinal direction remains constantly poor for increasing energies and a given reflection. The work demonstrates that, even for high-energy X-rays, length scales in the 10 µm range can be accessed easily since the macroscopic scale has to be compared with the large *Pendellösung* periods and thus the narrow intrinsic line widths of high-energy X-rays in the Laue case. In addition, apart from the very special case of anomalous transmission, Laue geometry has the advantage of equal attenuation through all beam paths, whereas in the Bragg case deeply buried layers contribute differently from those near the surface.

Of course, the transverse resolution is strongly affected by the mosaic spread of the sample and the presented

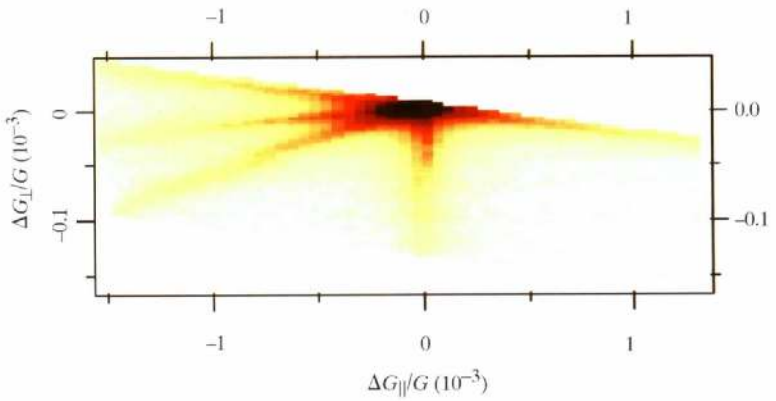

Figure 8
Measured reciprocal-space mapping around the 220 reflection at 125 keV. The resolution for the expected satellites is insufficient which smears them out to the additional pure longitudinal stripe lying symmetrically between the monochromator and the analyzer streaks.

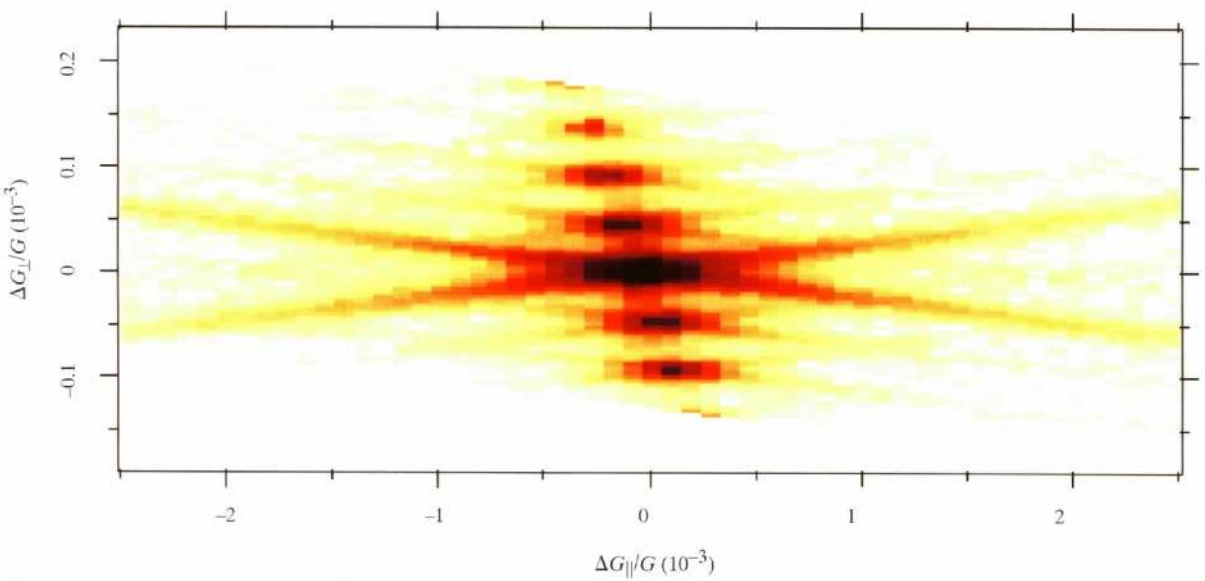

Figure 9
Experimental reciprocal-space mapping around the $11\bar{1}$ reflection at 80 keV. Satellites lying on a line in the $\xi\xi 0$ direction are perfectly resolved and show individual resolution streaks. The scale is the same as in the previous mappings.

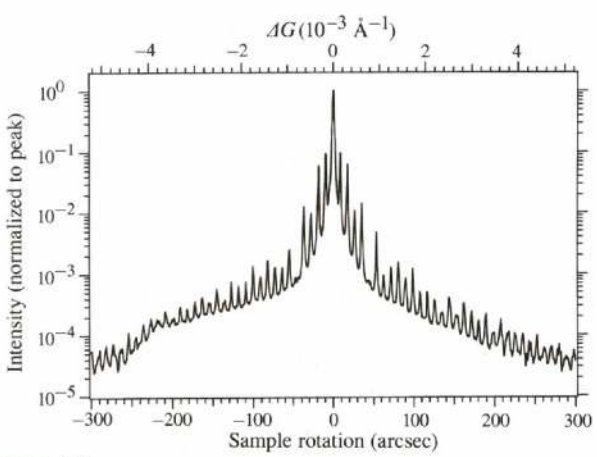

Figure 10
2 × 32 satellites around the $11\bar{1}$ Bragg position obtained in the two-crystal mode at 80 keV. The oscillations are far from being damped at the end of the scan range.

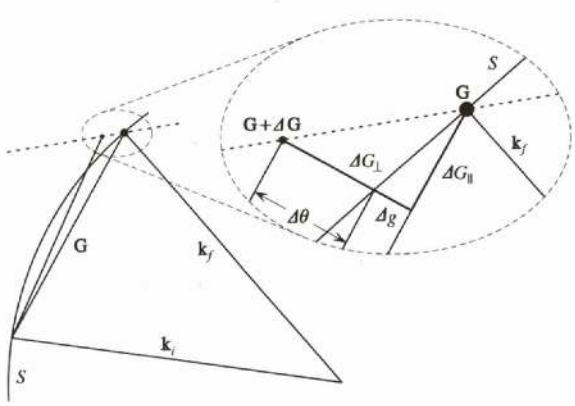

Figure 11
Situation in reciprocal space for the measurement in the two crystal mode. The magnification around the reciprocal-lattice point, **G**, shows the quantities for the calculation of the distance ΔG to the neighbouring satellite from the rotation angle $\Delta\theta$.

method will not work for non-perfect samples. In this case one has to consider the intrinsic longitudinal resolution given by equation (8).

From the point of view of sample characterization we have seen 64 satellite reflections around the $11\bar{1}$ atomic Bragg position, the distance between neighbours being 9.0″ corresponding to a real-space dimension of d = 4.0 μm. This agrees perfectly with the periodicity of the macro structure of the direction considered. The observation of satellites, however, contains more information than visual light or small-angle X-ray and neutron diffraction, since it demonstrates the atomic coherence in the macro lattice! Light and small-angle interferences can be obtained from both crystalline and amorphous bulk material, whereas an underlying Bragg reflection arises from the periodic structure on the atomic scale.

The authors wish to thank Andreas Magerl and Ulrike Grüning for providing the sample produced by Siemens AG.

References

Bouchard, R., Kouptsidis, S., Neumann, H.-B., Schmidt, T. & Schneider, J. R. (1993). *J. Appl. Phys.* **73**(8), 3680–3684.

Chattopadhyay, T., Liss, K.-D. & Tschentscher, T. (1997). *ESRF Highlights 1996/1997*, p. 19. ESRF, Grenoble, France.

Grüning, U., Lehmann, V. & Eberl, U. (1996). *Phys. Bl.* **52**(7/8), 661–664.

Grüning, U., Lehmann, V., Ottow, S. & Busch, K. (1996). *Appl. Phys. Lett.* **68**(6), 747–749.

Helmers, L. (1996). Dissertation, Rheinisch Westfälische Technische Hochschule Aachen, Germany.

Lippert, M., Brückel, T., Köhler, T. & Schneider, J. R. (1994). *Europhys. Lett.* **27**(7), 537–541.

Liss, K.-D. (1994). Dissertation, Rheinisch Westfälische Technische Hochschule Aachen, Germany.

Liss, K.-D., Magerl, A., Hock, R. & Remhof, A. (1996). *ESRF Highlights 1995/1996*, pp. 46–47. ESRF, Grenoble, France. http://www.esrf.fr/highlights/Science/Mater.htm#mat5. http://www.esrf.fr/exp_facilities/id15a/science/usw_1996/usw.html.

Liss, K.-D., Magerl, A., Hock, R., Remhof, A. & Waibel, B. (1997). *Europhys. Lett.* **40**(4), 369–374.

Liss, K.-D., Magerl, A., Remhof, A. & Hock, R. (1997). *Acta Cryst.* A**53**, 181–186.

Magerl, A., Liss, K.-D., Hastings, J. B., Siddons, D. P., Neumann, H.-B., Poulsen, H. F., Rütt, U., Schneider, J. R. & Madar, R. (1995). *Europhys. Lett.* **31**(5/6), 329–334.

Neumann, H.-B. (1991). Internal Report 91-06. HASYLAB, DESY, Hamburg, Germany.

Neumann, H.-B., Poulsen, H. F., Rütt, U., Schneider, J. R. & Zimmermann, M. v. (1995). *Phase Transit.* B**55**(1/4), 17–35.

Neumann, H. B., Rütt, U., Schneider, J. R. & Nagasawa, H. (1994). *J. Appl. Cryst.* **27**, 1030–1038.

Pick, M. A., Bickmann, K., Pofahl, E., Zwoll, K. & Wenzl, H. (1977). *J. Appl. Cryst.* **10**, 450–457.

Poulsen, H. F., Zimmermann, M. v., Schneider, J. R., Andersen, N. H., Schleger, P., Madsen, J., Hadfield, R., Casalta, H., Liang, R., Dosanjh, P. & Hardy, W. (1996). *Phys. Rev. B*, **53**(22), 15335–15344.

Rauch, H. & Petrascheck, D. (1976). *Grundlagen für ein Laue-Neutroneninterferometer, Teil 1: Dynamische Beugung.*, AIAU 74405b. Wein: Atominstitut der Österreichischen Universitäten.

Rauch, H. & Petrascheck, D. (1978). *Dynamical Neutron Diffraction and its Application in Neutron Diffraction*, edited by H. Dachs, pp. 303–351. Berlin: Springer-Verlag.

Royer, A. & Bastie, P. (1997). *Scr. Mater.* **36**(10), 1151–1159.

Royer, A., Bastie, P. & Véron, M. (1997*a*). *Scr. Mater.* **37**(8), 1199–1201.

Royer, A., Bastie, P. & Véron, M. (1997*b*). *Mater. Sci. Eng.* A**234**/**236**, 1110–1113.

Rütt, U., Neumann, H.-B., Poulsen, H. F. & Schneider, J. R. (1995). *J. Appl. Cryst.* **28**, 729–737.

Shen, Q. (1996). *Synchrotron Rad. News*, **9**(3), 24–29.

Shen, Q. & Kycia, S. (1997). *Phys. Rev. B*, **55**(23), 15791–15797.

Strempfer, J., Brückel, T., Rütt, U., Schneider, J. R., Liss, K.-D. & Tschentscher, T. (1996). *Acta Cryst.* A**52**, 438–449.

Suortti, P. & Tschentscher, T. (1995). *Rev. Sci. Instrum.* **66**(2), 1798–1801.

Zachariasen, W. H. (1945). *Theory of X-ray Diffraction in Crystals*. London: Wiley.

Zhukov, S. G., Chernyshev, V. V., Aslanov, L. A., Vakhrushev, S. B. & Schenk, H. (1995). *J. Appl. Cryst.* **28**, 385–391.